Microcrack-induced strain relief in GaN/AlN quantum dots grown on Si(111)

G. Sarusi, O. Moshe, S. Khatsevich, and D. H. Rich
Department of Physics, The Ilse Katz Center for Nano and Meso Scale Science and Technology, Ben-Gurion University of the Negev, P.O. Box 653, Beer-Sheva 84105, Israel

B. Damilano
Centre de recherché sur l'Hetero-Epitaxie et ses Applications, Centre National de la Recherche, Rue B. Gregory, Sophia Antipolis, 06560 Valbonne, France

(Received 24 October 2006; revised manuscript received 5 December 2006; published 6 February 2007)

The optical properties of vertically stacked self-assembled GaN/AlN quantum dots (QD's) grown on Si substrates were studied by means of temporally and spatially resolved cathodoluminescence (CL). An analysis of the CL spectra, thermal activation energies, and measured decay times of the QD luminescence was performed near stress-induced microcracks, revealing changes in the optical properties that can be attributed to stress-dependent variations in the band edges, the polarization field, and the oscillator strength between electrons and holes. Three-dimensional 6×6 $\boldsymbol{k}\cdot\boldsymbol{p}$ calculations of the QD electron and hole wave functions and eigenstates were performed to examine the influence of biaxial and uniaxial stresses on the optical properties in varying proximity to the microcracks.

DOI: 10.1103/PhysRevB.75.075306 PACS number(s): 78.67.Hc, 78.66.Fd, 73.21.La, 78.60.Hk

I. INTRODUCTION

The vast potential in high-quality light emitters in the visible to ultraviolet spectral range is the main motivation behind the interest in III-nitride quantum dot (QD) systems. AlN/GaN QD's are promising structures for variable-wavelength devices possessing a high luminescence efficiency.[1–3] A large difference in the band gap energies between GaN (3.4 eV) and AlN (6.2 eV) enables GaN/AlGaN self-assembled QD's to be ideal candidates for tunable room-temperature light-emitting devices.[1,4,5] Another important property of the GaN/AlN QD system is the huge electric field induced by polarization differences, estimated at $\sim$5.5–7 MV/cm, often present in the (0001) growth direction.[6–8] The field is the source of a quantum-confined Stark effect that induces a strong redshift in the excitonic luminescence spectra and lowers the QD excitonic transition energy to a value well below the GaN bulk transition energy.[2,3]

In this study, the optical properties of vertically stacked self-assembled GaN/AlN QD's grown on Si(111) substrates were examined with temporally and spatially resolved cathodoluminescence (CL). While the presence of thermal stress-induced microcracks is clearly undesirable when attempting to obtain high-quality thin-film growth of III-nitride films and QD's on Si substrates, the presence of microcracking, however, enables a study of potentially interesting stress-induced energy shifts and lifetime changes in the QD optical transitions that can be measured with a high-resolution spatially resolved probe, such as with CL. Normally, it is difficult to locally perturb the strain tensor of QD's in a reliable and reproducible way, and we have found such a way using microcracks. While stress variations induced by microcracks in the $Al_xGa_{1-x}N$/GaN system were previously studied thoroughly with spatially and spectrally resolved CL,[9] we present the first application of such stress variations to GaN/AlN QD's in this paper. We further present a model of these results by using three-dimensional (3D) 6×6 $\boldsymbol{k}\cdot\boldsymbol{p}$ calculations of the eigenstates of the GaN/AlN QD's in varying proximity to the microcracks.

II. EXPERIMENTAL DETAILS

The samples were grown by molecular beam epitaxy using the 2D to 3D Stranski-Krastanov growth-mode transition.[10,11] Both samples were grown on Si (111) substrates and consist of AlN (30 nm)/GaN (400 nm)/AlN (700 nm) buffer layers followed by either 40 or 85 layers of GaN QD's, labeled as samples S-40 and S-85, respectively. The growth of sample S-40 (S-85) involved 18-nm- (6.7-nm-) thick AlN barrier layers with 2.6-nm- (1.6-nm-) thick GaN dot layers, resulting in an average dot height of $\sim$5 nm ($\sim$3.7 nm), as determined previously by transmission electron microscopy (TEM) measurements.[12] Both samples were terminated with a 40-nm-thick AlN capping layer. The average dot density is $\sim5\times10^{-11}$ cm^{-2}.[12]

CL experiments were performed with a modified JEOL-5910 scanning electron microscope (SEM). The luminescence was collected with a copper ellipsoidal mirror and transferred to a 1/4-m monochromator via a flexible solarization-resistant ultraviolet optical fiber bundle that was designed for insertion into the SEM vacuum chamber. The dispersed light was detected with a multialkali photomultiplier tube which enabled photon counting. The sample was cooled with a closed-cycle liquid He system connected to the SEM sample stage by a copper braid. The sample temperature was varied from 50 K to 300 K. Time-resolved CL experiments were performed with the method of delayed coincidence in an inverted single-photon counting mode, with a time resolution of $\sim$100 ps.[13] Electron beam pulses of 50 ns width with a 100-kHz repetition rate were used to excite the sample.

 ©2007 The American Physical Society

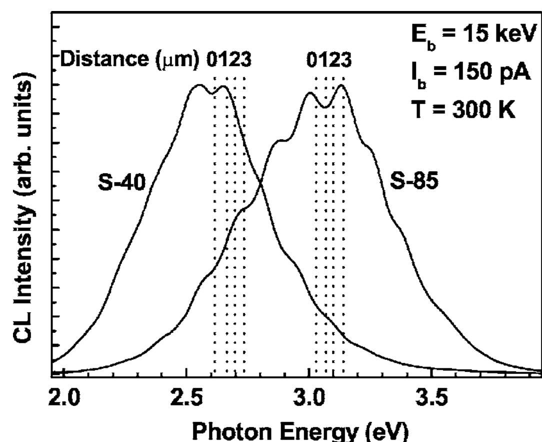

FIG. 1. Spatially integrated CL spectra of the S-40 and S-85 QD samples at $T=300$ K. The beam current I_b and electron-beam energy E_b were 150 pA and 15 keV, respectively. The resulting calculated values of E_x are shown by the four vertical dotted lines for each sample which indicate distances of 0, 1, 2, and 3 μm from the microcrack of each sample.

III. THEORETICAL CALCULATIONS USING A THREE-DIMENSIONAL $k \cdot p$ METHOD

The electron and hole wave functions and eigenstates were obtained with 3D 6×6 $\boldsymbol{k} \cdot \boldsymbol{p}$ calculations using the NEXTNANO3 quantum device simulation software.[14] The calculations utilized a 3D Schrödinger equation for wurtzite materials including strain, deformation potentials, and piezoelectric and pyroelectric charges, the latter of which accounts for the polarization field. The choice of the pyroelectric (spontaneous) constants P_{sp} will have an appreciable effect on the resulting electric field in the QD. We employed the material parameters used previously for calculations of the polarization field and eigenstates in GaN/AlN QD's,[15–17] although other values for the material parameters, including those for P_{sp}, have been obtained and used in the literature.[18–20] The fully strained GaN/AlN QD's were simulated by minimization of the elastic energy within a continuum model approach that takes into account the symmetry of the hexagonal crystal structure. External stresses ranging from purely biaxial to uniaxial were used to simulate the thermal stress in varying proximity to the microcracks. In order to calculate the wave functions, a single-band model for the electrons and a six-band $\boldsymbol{k} \cdot \boldsymbol{p}$ Hamiltonian for the holes were employed. The coupling between the conduction and valence bands was neglected, owing to the size of the GaN and AlN band gaps.[20]

IV. RESULTS AND DISCUSSION

A. Cathodoluminescence imaging and spectroscopy

Spatially integrated CL spectra of the two samples are shown in Fig. 1. The center of gravity of the excitonic luminescence lies at an energy lower than that of GaN bulk. Confinement conditions are expected to give rise to higher excitonic transition energies E_x. However, the strong polarization field causes the excitonic transition energy to shift in the opposite direction. Compressive stress acting on the GaN QD, owing to the mismatch in the lattice constants between GaN and AlN ($a_{GaN}=3.189$ Å and $a_{AlN}=3.112$ Å), increases the GaN band gap but it is the Stark effect that decreases it strongly, even below the unstrained GaN band gap. The CL spectrum for sample S-85 is centered at a higher energy than that for sample S-40, as the smaller average dot size for S-85 is expected to lead to larger *e*-*h* confinement energies. A shift of ~500 meV is observed between the centers of the two peaks in Fig. 1. We also note here that the excitonic peak energy positions E_x for both samples are approximately independent of the *e*-beam position relative to the cracks. Moreover, the strain in the QD stack is affected strongly by the average Al and Ga compositions.[21] The tensile strain of the AlN matrix in the QD stack is expected to be larger in S-85 in comparison to that for S-40, owing to the greater average Ga composition in the QD stack of S-85. Therefore, the compressive strain acting on the GaN QD's is likewise smaller in S-85, resulting in a smaller polarization field and larger E_x for the QD's in sample S-85 relative to that for S-40.

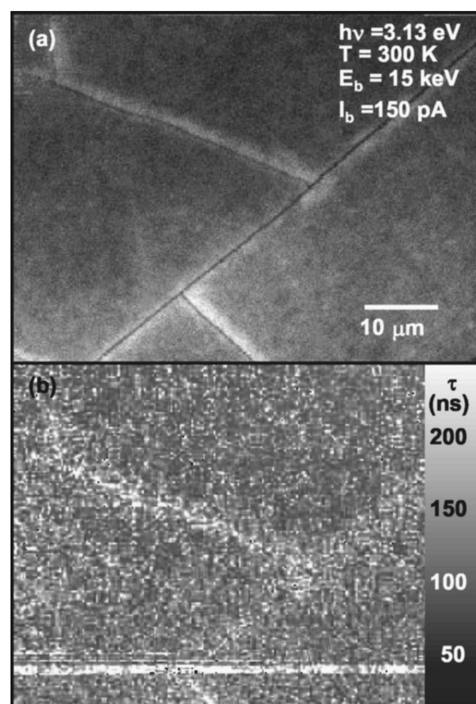

FIG. 2. Monochromatic CL image (a) and CL decay time image (b) of sample S-85. The beam current I_b and electron-beam energy E_b were 150 pA and 15 keV, respectively, for the CL imaging. The gray scale bar represents the mapping of the decay time τ in (b).

Due to the large difference in thermal expansion coefficient between III-nitrides and Si, microcracks form in the III-nitride epilayer as a result of thermal cycling from growth to lower temperatures.[22] The microcracks help relieve the large tensile stress acting on the AlN/GaN layers. A monochromatic CL image of the S-85 sample in Fig. 2(a) shows the presence of dark line defects (DLD's) when the imaging energy is set to E_x—i.e., the peak of the QD excitonic energy. The DLD's result from nonradiative recombination at the microcracks. An analysis of the CL imaging shows an in-

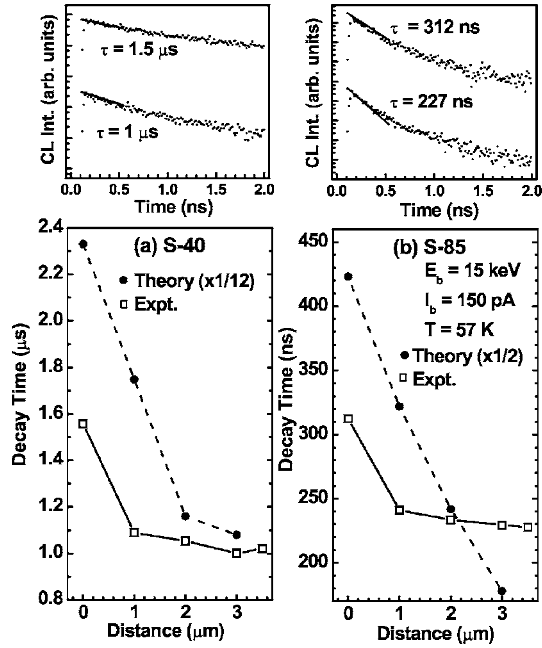

FIG. 3. The decay time τ as a function of distance from a microcrack for samples S-40 (a) and S-85 (b). Time decay curves in a semilogarithmic plot (upper panel) are shown for e-beam positions both near and far from the crack (distances of ~0 and ~3 μm, respectively, for the top and bottom curves). The calculated radiative decay time τ_R is also plotted in (a) and (b) to illustrate an agreement between theory and experiment with regards to relative changes in lifetime for various distances from the microcrack. The values for τ_R (theory) are reduced by factors of 12 and 2 in (a) and (b), respectively, to enable a comparison between theory and experiment.

crease in CL intensity when the e-beam approaches within ~3 μm of the cracks. The thermally induced cracks created after growth act to change the stress tensor form from biaxial tensile stress far from the crack to nearly uniaxial tensile stress in close proximity to the microcrack.[23] Since the microcracks were formed well after growth, the QD size and shape distribution remains unaffected by changes in the external stress on the AlN matrix and QD stack. The presence of this external stress variation further enables an examination of stress-induced changes in the optical properties of the QD's and the attendant confinement of electrons and holes.

B. Time-resolved CL and imaging of the decay time

Time-resolved measurements of the decay of the excitonic QD luminescence were performed, and results are shown in Figs. 2(b) and 3. At positions far from the microcracks, decay times of ~230 ns and ~1 μs were measured for samples S-85 and S-40, respectively. These long decay times are attributed to the large spatial separation between electrons and holes, as caused by the polarization field in the QD's.[24] Our calculations show that the electron wave function is centered near the top of the truncated pyramid and the hole wave function is localized just beneath the wetting layer. Upon further examination, an increase in decay time by about 50% for both samples occurs when the e-beam approaches the microcrack, as shown in Fig. 3, suggesting a smaller wave function overlap near the cracks. An image showing a map of the decay time is shown in Fig. 2(b). The image was obtained over the same region as the monochromatic CL image of Fig. 2(a) by acquiring a set of discrete monochromatic CL images containing 320×240 pixels at different time windows relative to the decay edge of the exciting pulse. The decay time τ at each pixel was obtained by a linear fit to $\exp(-t/\tau)$ over the corresponding pixels in all discrete images. A clear ~50% increase in the decay time is illustrated by bright lines in the time decay image of Fig. 2(b) that correlate with the positions of the microcracks in the monochromatic CL image of Fig. 2(a).

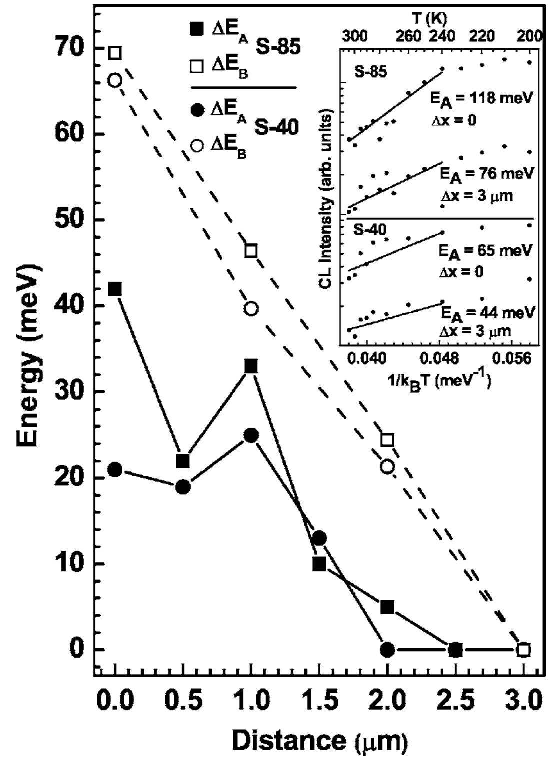

FIG. 4. The change in the activation energy, ΔE_A, vs distance from a microcrack for samples S-40 and S-85. The average change in band edge relative to the QD e-h levels, ΔE_B, from the calculations is also shown as a function of distance to illustrate the strong correlation with ΔE_A, which is referenced to the biaxially stressed regions far from the microcracks. The logarithm of the integrated QD emission intensity vs $1/k_BT$ for samples S-40 and S-85, from which E_A is determined, is shown in the inset for e-beam positions both near and far from the microcrack (distances Δx of ~0 and ~3 μm, respectively).

C. Thermal quenching of the luminescence

By examining the change in the integrated QD excitonic emission intensity, $I(T)$, as a function of temperature, the activation energy (E_A) for the thermal quenching of luminescence near room temperature can be determined from the slopes of the Arrenhius semilogarithmic plots using $I(T) = I_0 \exp(E_A/k_BT)$.[25] Thermal quenching measurements of the samples resulted in activation energies of ~44 meV and

~76 meV for samples S-40 and S-85, respectively, in the biaxially stressed regions far from the microcracks, as shown in the inset of Fig. 4. As the *e*-beam is scanned towards the microcracks, E_A increases to values of ~65 meV and ~118 meV for S-40 and S-85, respectively, for distances near the microcrack, as shown in Fig. 4. Thermal activation generally reflects the thermal energy required to remove confined carriers over a barrier before they can recombine radiatively. The change in E_A is thus likely connected to stress-induced changes in the AlN conduction and valence band edges relative to the ground-state *e*-*h* levels in the QD (i.e., $\Delta E_{c,e}$ and $\Delta E_{v,h}$), as a reduced tensile stress near the microcracks will lead to an increased AlN band-gap energy. $\Delta E_{c,e}$ and $\Delta E_{v,h}$ are defined as the energy differences between the AlN conduction and valence band edges and the QD ground-state electron and hole levels, respectively. We note that the enhanced luminescence efficiency near the cracks in the CL images of Fig. 2 is also consistent with a larger barrier height that enhances carrier capture and reduces thermal reemission. We cannot, however, preclude the possibility of a variation of geometrical emission conditions within the microcrack regions.

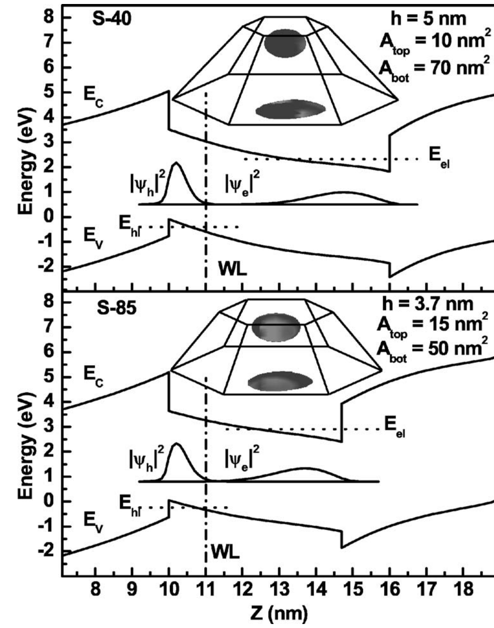

FIG. 5. The band-edge profile along the z direction (growth direction) for the model truncated pyramidal QD's of the S-40 and S-85 samples at $T=300$ K. The geometric parameters of height and areas for the top and bottom faces for each pyramid are indicated. The probability densities for the electron and hole wave functions integrated over the *x*-*y* plane, $|\psi_{e,h}(z)|^2$, are shown to illustrate the expected small wave function overlap. A 3D representation of the QD truncated pyramid and *isosurfaces* of the *e*-*h* wave functions for $|\psi_e(\mathbf{r})|^2=0.5$ and $|\psi_h(\mathbf{r})|^2=0.15$ are illustrated in the insets.

D. Determination of the uniaxial and biaxial stress in the QD layers

In order to test the various hypotheses involving activation energy, carrier decay time, and strain-induced changes in the polarization field, we now present the results of the 3D $\mathbf{k}\cdot\mathbf{p}$ calculations. The isolated QD in our model is a single GaN truncated hexagonal pyramid situated on a 1-nm-thick wetting layer (WL) and embedded in an AlN matrix. The average QD heights and volumes are known from previous TEM investigations of these samples and are 5.0 nm and 520 nm^3 and 3.7 nm and 320 nm^3, respectively, for samples S-40 and S-85.[12] In our model, we have constrained these heights and volumes to be constants in our calculations while allowing the area of both the top and bottom square faces of the truncated pyramid to vary independently. Essentially, the aspect ratio of the pyramid was varied in order to enable fits of the calculated *e*-*h* transition energies E_x to the experimental values determined from the CL spectra of Fig. 1. Using these assumptions, the QD pyramidal aspect ratio and the AlN strain components were changed in a series of simulations in order to determine the resulting uniaxial stress near the crack and biaxial stress far from the crack in the AlN barrier for both samples. For an in-plane biaxial tensile stress ($\sigma_{xx}=\sigma_{yy}=S_b$, $\sigma_{zz}=0$) on an AlN film, the strain components are given by $\varepsilon_{xx}=\varepsilon_{yy}=(C_{11}+C_{12}-2C_{13}{}^2/C_{33})^{-1}S_b$ and $\varepsilon_{zz}=(2C_{13}/C_{33})\varepsilon_{xx}$,[26] where the elastic constants are given by Wright as $C_{11}=3960$, $C_{12}=1370$, $C_{13}=1080$, and $C_{33}=3730$ kbar.[19,27] Similarily, near the microcrack, an in-plane uniaxial stress ($\sigma_{xx}=S_u$, $\sigma_{yy}=\sigma_{zz}=0$) is expected in which $S_u\approx S_b$, where S_b and S_u represent the magnitude of the biaxial and uniaxial stresses, respectively, in the AlN film.

By performing a series of iterations that involved calculating the strain tensor components, energies E_x, $\Delta E_{c,e}$, and $\Delta E_{v,h}$, and QD *e*-*h* wave functions for the complete truncated pyramidal model system as a function of biaxial and uniaxial stress in the AlN barriers, we obtained biaxial tensile stress values S_b of ~30 kbar and ~15 kbar at room temperature for samples S-85 and S-40, respectively. The resulting calculated values of E_x are shown in Fig. 1 by the four vertical dotted lines for each sample which indicate distances of 0, 1, 2, and 3 μm from the microcrack of each sample. The magnitudes of the stress values are consistent with previous results obtained in the literature for III-nitride films grown on Si.[22] As expected, a reduced tensile stress in the AlN barrier is found in sample S-40 relative to S-85 as a result of the reduced average Ga composition in S-40 relative to that for S-85. Since the change in stress tensor, when moving from regions of biaxial stress (greater than ~3 μm from the cracks) to uniaxial stress very near the crack, results in corresponding changes in $\Delta E_{c,e}$ and $\Delta E_{v,h}$, we plot the average change in the band edge, ΔE_B, where $E_B=(\Delta E_{c,e}+\Delta E_{v,h})/2$, as a function of distance from the crack in Fig. 4 to compare with the change in the activation energy, ΔE_A, referenced to the biaxially stressed regions far from the microcracks. A strong correspondence in behavior between ΔE_B and ΔE_A versus distance from the microcrack is demonstrated in Fig. 4. This further supports our initial hypothesis that changes in the thermal activation are associated with changes in the AlN barrier band edges relative to the QD *e*-*h* levels, owing to deep level defects in the AlN matrix that are responsible for the thermal quenching of the luminescence.

E. Calculation of the radiative lifetime and comparison with the CL decay time

Due to the large polarization fields, the electron wave function is localized near the top of the QD and the holes at the WL under the QD,[28] as shown in Fig. 5. The larger QD (structure of sample S-40) clearly shows a reduced energy separation between single-particle electron and hole levels in the band profile of Fig. 5 that is expected to lead to the observed spectral redshift of ~500 meV relative to emission from sample S-85. The calculated excitonic transition energies E_x as a function of distance for the microcracks are shown for both samples in Fig. 1. The reduction in E_x for sample S-40 is therefore mainly due to the larger distance over which the polarization field acts on electrons and holes. Isosurfaces of the *e-h* wave functions are also illustrated in Fig. 5 for both QD structures.

We can estimate the rate of radiative recombination by calculating the oscillator strength of the exciton:[20]

$$f = \frac{2\hbar^2}{m_0 E_x} \sum_l \left| \int d^3 r \psi_e^*(\vec{r}) \left(\hat{e} \cdot \frac{1}{i} \vec{\nabla} \right) \psi_h^{(l)}(\vec{r}) \right|^2, \quad (1)$$

where $\hat{e}$ is the polarization of the emitted light and the index l denotes a sum over degenerate hole levels possessing different spin configurations. In this calculation, we further average f over the three orthogonal polarization directions. The total electron and hole wave functions are each composed of envelope, Bloch, and spin components. The evaluation of the integrals in Eq. (1) further requires calculating integrals over the unit cells involving the Bloch *s*- and *p*-like wave functions, [i.e., $u_s(\boldsymbol{r})$ and $u_p^{(j)}(\boldsymbol{r})$, respectively] for the conduction and valence states as

$$\int d^3 r u_s(\vec{r}) \frac{\partial}{\partial x_i} u_p^{(j)}(\vec{r}) = \delta_{i,j} \sqrt{\frac{m_0 E_P}{2\hbar^2}}, \quad (2)$$

where $\delta_{i,j}$ is the Kronecker delta (i,j vary from 1 to 3) and E_p is the Kane energy, which we take as 14.0 eV.[19] The total hole wave function $\psi_h(\boldsymbol{r})$ can be expressed as a combination of the basis Bloch functions for which the 6×6 $\boldsymbol{k}\cdot\boldsymbol{p}$ Hamiltonian was diagonalized as follows:

$$\psi_h(\vec{r}) = \sum_k \sum_j F_{kj}(\vec{r}) u_p^{(j)}(\vec{r}) s_k, \quad (3)$$

where s_k (k=0 or 1) represent the two orthogonal spin wave functions and $F_{kj}(\boldsymbol{r})$ are the six envelope functions that are obtained from the diagonalization. Similarily, the two degenerate ground-state electron wave functions $\psi_e(\boldsymbol{r})$ are given by

$$\psi_e(\vec{r}) = \varphi(\vec{r}) u_s(\vec{r}) s_k, \quad (4)$$

where $\varphi(\boldsymbol{r})$ is the electron envelope function obtained from the 3D single-band effective-mass calculation. The oscillator strength f was therefore calculated by substitution of Eqs. (3) and (4) into Eq. (1) and by using the conditions of Eq. (2) for integrating the Bloch functions over a unit cell. The radiative lifetime is then inversely proportional to the oscillator strength and determined by the following expression:[29]

$$\tau_R = \frac{2\pi\varepsilon_0 m_0 c^3 \hbar^2}{n e^2 E_x^2 f}, \quad (5)$$

where the fundamental constants ε_0, m_0, c, $\hbar$, and e have their usual meaning and n is the refractive index of GaN, which we take as 2.29 from Ref. 30.

Further consistency in these calculations is demonstrated by plotting the calculated radiative lifetime τ_R versus distance in Fig. 3 to compare with the measured decay times τ. The relative increase in τ_R for positions approaching the microcracks is consistent with a ~50% increase in measured decay time near the microcrack for both samples. The calculations show a factor of ~2 increase in the radiative lifetime for each QD structure as the position is moved from a point far from to a point near the microcracks. The calculations also predict a larger τ_R, by factors ranging from 1.6 to 2.7, than the values of τ measured for sample S-85. A much larger deviation between experiment and theory is observed for sample S-40, in which an order-of-magnitude greater lifetime is predicted from the theory in Fig. 3(a). Since the predicted lifetimes range from ~13 to 28 μs and are much greater than the measured decays time of ~1–1.6 μs for sample S-40, we hypothesize that a nonradiative path associated with defect levels in the barrier and with the observed thermal quenching of luminescence is responsible for the reduction in the measured decay time for this sample, and to a lesser extent for sample S-85. This argument is supported again by the correlation between the average change in the band edge (ΔE_B) and the change in the activation energy (ΔE_A) for thermal quenching of the luminescence for various positions approaching a microcrack (as shown in Fig. 4) which confirms the existence of such nonradiative defect states within the gap of the AlN barrier. Since the calculated radiative lifetime is much shorter for the structure of sample S-85, these defect levels should have a reduced effect on the measured total decay time τ for this sample, as observed. Thus, the calculated relative changes in τ_R caused by the strain-induced changes in the polarization field in the transition from regions of biaxial to uniaxial stress are in agreement with the experimental decay time measurements for both samples.

V. SUMMARY AND CONCLUSIONS

In conclusion, the effects of microcrack-induced stress changes on GaN/AlN QD's were studied by spatially and temporally resolved CL. Three-dimensional 6×6 $\boldsymbol{k}\cdot\boldsymbol{p}$ calculations of the QD electron and hole wave functions and eigenstates were performed to examine the influence of biaxial and uniaxial stresses on the optical properties in varying proximity to the microcracks. A reduction of tensile stress in the AlN barrier increases the compressive stress in the GaN dot, resulting in a larger polarization field, larger calculated radiative decay time, and longer measured decay times. The change in stress also enhances the *e-h* confinement within the QD and produces a more efficient trapping

of carriers that leads to a higher thermal activation energy and higher luminescence efficiency near the microcracks. The oscillator strengths and radiative lifetimes as a function of distance from the microcracks were calculated and compared with the measured decay times. For positions approaching the microcrack, the relative changes in the calculated radiative lifetime are consistent with the relative changes in the measured decay times, which showed an increase of ~50% near the microcracks.

ACKNOWLEDGMENT

This work was supported in part by the Israel Science Foundation (ISF Grant No. 8/02-1).

[1] S. Tanaka, H. Hirayama, Y. Aoyagi, Y. Narukawa, Y. Kawakami, and S. Fujita, Appl. Phys. Lett. **71**, 1299 (1997).
[2] B. Damilano, N. Grandjean, F. Semond, J. Massies, and M. Leroux, Appl. Phys. Lett. **75**, 962 (1999).
[3] B. Damilano, N. Grandjean, J. Massies, and F. Semond, Appl. Surf. Sci. **164**, 241 (2000).
[4] Y. Arakawa and H. Sakaki, Appl. Phys. Lett. **40**, 939 (1982).
[5] S. Nakamura, S. Pearton, and G. Fasol, *The Blue Laser Diode* (Springer, New York, 2000).
[6] F. Bernardini, V. Fiorentini, and D. Vanderbilt, Phys. Rev. B **63**, 193201 (2001).
[7] F. Bechstedt, U. Grossner, and J. Furthmuller, Phys. Rev. B **62**, 8003 (2000).
[8] F. Bernardini, V. Fiorentini, and D. Vanderbilt, Phys. Rev. Lett. **79**, 3958 (1997).
[9] D. Rudloff, T. Riemann, J. Christen, Q. K. K. Liu, A. Kaschner, A. Hoffmann, Ch. Thomsen, K. Vogeler, M. Diesselberg, S. Einfeldt, and D. Hommel, Appl. Phys. Lett. **82**, 367 (2003).
[10] S. Kako, M. Miyamura, K. Tachibana, K. Hoshino, and Y. Arakawa, Appl. Phys. Lett. **83**, 984 (2003).
[11] B. Daudin, F. Widmann, G. Feuillet, Y. Samson, M. Arlery, and J. L. Rouviere, Phys. Rev. B **56**, R7069 (1997).
[12] S. Kalliakos, T. Bretagnon, P. Lefebvre, T. Taliercio, B. Gil, N. Grandjean, B. Damilano, A. Dussaigne, and J. Massies, J. Appl. Phys. **96**, 180 (2004).
[13] H. T. Lin, D. H. Rich, A. Konkar, P. Chen, and A. Madhukar, J. Appl. Phys. **81**, 3186 (1997).
[14] K. H. Lee, J. H. Na, R. A. Taylor, S. N. Yi, S. Birner, Y. S. Park, C. M. Park, and T. W. Kang, Appl. Phys. Lett. **89**, 023103 (2006).
[15] I. Vurgaftman and J. R. Meyer, J. Appl. Phys. **94**, 3675 (2003).
[16] O. Ambacher, J. Majewski, C. Miskys, A. Link, M. Hermann, M. Eickhoff, M. Stutzmann, F. Bernardini, V. Fiorentini, V. Tilak, B. Schaff, and L. F. Eastman, J. Phys.: Condens. Matter **14**, 3399 (2002).
[17] D. P. Williams, A. D. Andreev, E. P. O'Reilly, and D. A. Faux, Phys. Rev. B **72**, 235318 (2005); D. P. Williams, A. D. Andreev, and E. P. O'Reilly, *ibid.* **73**, 241301(R) (2006).
[18] F. Bernardini, V. Fiorentini, and D. Vanderbilt, Phys. Rev. B **56**, R10024 (1997).
[19] I. Vurgaftman, J. R. Meyer, and L. R. Ram-Mohan, J. Appl. Phys. **89**, 5815 (2001).
[20] V. A. Fonoberov and A. A. Balandin, J. Appl. Phys. **94**, 7178 (2003); J. Vac. Sci. Technol. B **22**, 2190 (2004).
[21] G. Salviati, F. Rossi, N. Armani, V. Ggrillo, O. Martinez, A. Vinattierei, B. Damilano, A. Matsuse, and N. Grandjean, J. Phys.: Condens. Matter **16**, S15 (2004).
[22] G. Sarusi, O. Moshe, S. Khatsevich, D. H. Rich, J. Salzman, B. Meyler, M. Shandalov, and Y. Golan, J. Electron. Mater. **35** (12), L15 (2006).
[23] D. H. Rich, A. Ksendzov, R. W. Terhune, F. J. Grunthaner, B. A. Wilson, H. Shen, M. Dutta, S. M. Vernon, and T. M. Dixon, Phys. Rev. B **43**, 6836 (1991).
[24] V. Ranjan, G. Allan, C. Priester, and C. Delerue, Phys. Rev. B **68**, 115305 (2003).
[25] S. Khatsevich, D. H. Rich, E. T. Kim, and A. Madhukar, J. Appl. Phys. **97**, 123520 (2005).
[26] J. M. Wagner and F. Bechstedt, Phys. Status Solidi B **234**, 965 (2002).
[27] A. F. Wright, J. Appl. Phys. **82**, 2833 (1997).
[28] A. D. Andreev and E. P. O'Reilly, Phys. Rev. B **62**, 15851 (2000).
[29] G. W. Hooft, W. A. J. A. van der Poel, L. W. Molenkamp, and C. T. Foxon, Phys. Rev. B **35**, 8281 (1987).
[30] E. Ejder, Phys. Status Solidi A **6**, 445 (1971).